RSC Advances

PAPER

View Article Online
View Journal | View Issue

Cite this: *RSC Adv.*, 2024, **14**, 20426

Micropatterned superhydrophobic meshes coated with low-cost carbon nanoparticles for efficient oil/water separation†

Muhammad Qasim,[ab] Asghar Ali[a] and Ali Alnaser *[acd]

Received 3rd May 2024
Accepted 12th June 2024

DOI: 10.1039/d4ra03275f

rsc.li/rsc-advances

Superhydrophobic and superoleophilic meshes have gained considerable attention in oil/water separation in recent years. To fabricate such meshes, surface roughness features can be introduced, and the surface free energy can be lowered, preferably, by utilizing low cost, safe, and readily available materials. Herein, we report a novel approach for fabricating a superhydrophobic copper mesh using low-cost carbon nanoparticles embedded within surface micropatterns. To create the micropatterns, a femtosecond laser was employed. The fabricated mesh exhibited a water contact angle of 168.9° and a roll-off angle of only 5.9°. Additionally, the mesh was highly durable and effectively retained its superhydrophobicity during water jet impact and tape-peeling tests. After 50 cycles of the water jet impact test and 5 cycles of the tape-peeling test, the water contact angle reduced by only 0.3° and 2.3°, respectively. When tested for separating *n*-hexane/water mixtures, the mesh exhibited a separation efficiency of up to 98%. The separation efficiency remained essentially constant after 10 cycles of *n*-hexane/water separation. It was observed that the surface micropatterns played a significant role in achieving superhydrophobicity and imparting high durability to the mesh. Meshes lacking these laser-induced micropatterns showed higher wettability, lower durability, and decreased separation performance with repeated use.

1. Introduction

Separation of oil/water mixtures is a well-known research problem and represents an increasingly important and significant challenge in the industry. Oil/water mixtures can arise from the accidental release of oil and petroleum products during oil exploration, production, transportation, and storage as well as from oily wastewater produced across different industries including metal, food, and leather processing and oil and gas.[1] The adverse effects of oil spills and oily wastewater on the environment and the well-being of aquatic and terrestrial organisms, including humans, are well-documented.[2–5] For instance, short and long-term damages have been reported due to the blowout on the Deepwater Horizon oilrig that released 4.9 million barrels of crude oil into the Gulf of Mexico in 2010. This accidental release of oil destroyed local marine ecosystems, caused ecological changes, and resulted in elimination of rare species. In addition, over 53 species were threatened while many species of sharks and corals became nearly extinct.[6] Also, a long-term follow-up study revealed that people exposed to the oil during cleanup operations experienced prolonged or worsening illnesses even after 7 years of exposure.[7] Several methods have been developed and employed for oil/water separation including air flotation, filtration, coagulation, gravity settling, and oil-absorbing materials.[8,9] However, inherent limitations such as low separation efficiency, high cost, tedious operation, and/or secondary pollution necessitate the development of novel materials/systems for effective separation of oil and water.

Recently, significant research efforts have been directed towards oil/water separation using advanced surfaces obtained by adjusting the surface structure/roughness and/or the surface energy in order to achieve special wettability.[10,11] These surfaces, such as superhydrophobic/superoleophilic surfaces, show selectivity towards oil and water and can be effectively used to separate oil/water mixtures. Superhydrophobic surfaces, in general, exhibit water contact angle higher than 150° and sliding angle less than 10°.[12] With the presence of a hierarchical morphology consisting of micro/nanoscale roughness and low surface energy, a water drop on a superhydrophobic surface attains the Cassie wetting state where complete contact between the liquid and the surface becomes energetically unstable.[13] Superhydrophobic surfaces have been fabricated using sponges,[14] fabrics,[15] and meshes.[16] Among these,

[a]*Materials Science and Engineering Program, College of Arts and Sciences, American University of Sharjah, Sharjah 26666, United Arab Emirates. E-mail: aalnaser@aus.edu*

[b]*Department of Chemical and Biological Engineering, American University of Sharjah, Sharjah, 26666, United Arab Emirates*

[c]*Department of Physics, American University of Sharjah, Sharjah 26666, United Arab Emirates*

[d]*Materials Research Center, American University of Sharjah, Sharjah 26666, United Arab Emirates*

† Electronic supplementary information (ESI) available. See DOI: https://doi.org/10.1039/d4ra03275f

superhydrophobic metal meshes are an attractive option for oil/water separation owing to their porous structure, mechanical durability, low cost, and ease of availability.[17] Several methods have been proposed to impart superhydrophobicity to metal meshes by adding roughness and creating micro/nano roughness features. For instance, Ren *et al.*[18] used chemical agents to modify the surface of copper mesh *via* formation of $Cu(OH)_2$ nanoneedle arrays through immersion in aqueous solution of sodium hydroxide and ammonium persulphate. A coating of stearic acid was then applied to reduce the surface energy. The resulting mesh exhibited a water contact angle 157° and a roll-off angle of 5° and produced oil separation efficiency of more than 95%. Li *et al.*[19] used the spray coating process to coat attapulgite (APT) as the hydrophobic agent along with octadecyltrichlorosilane (OTCS) as low energy material and water-borne polyurethane (PU) as binder. The resulting mesh had a water contact angle as high as 158° and a roll-off angle as low as 8° while the oil separation efficiency was above 94%. Crick *et al.*[20] employed aerosol assisted chemical vapor deposition (CVD) to create rough microstructures on a copper mesh by coating with silicone elastomer (Sylgard 184). The resulting mesh exhibited a water contact angle as high as 167° with an oil separation efficiency of more than 99%. Wang *et al.*[21] used electrochemical deposition to roughen the surface of copper mesh followed by immersion in lauric acid solution to lower the surface energy. The resulting mesh was superhydrophobic with a water contact angle of 160°. Most of the time, the process of introducing surface roughness is technically complex or requires use of harsh chemicals. Also, different types of low surface energy materials have been utilized to impart superhydrophobicity to metal meshes. A common approach is to utilize silane agents (such as octadecyltrichlorosilane,[22] hexadecyltrimethoxysilane,[23] perfluorodecyltriethoxysilane,[24] 1*H*,1*H*,2*H*,2*H*-perfluorodecyl trimethoxysilane,[25] *etc.*). Although effective in lowering the surface energy, silane agents tend to be costly and, in case of fluorinated alkylsilanes, the health and environmental concerns pose serious limitations.[26,27] Therefore, to fabricate superhydrophobic metal meshes, there is a need to utilize low cost, safe, and readily available raw materials and develop simple yet effective methods to introduce surface roughness and lower the surface energy.

In the context of superhydrophobic surfaces, candle soot (CS) has recently emerged as a low-cost nanomaterial that is known for its convenient synthesis, production scalability, and low toxicity.[28,29] Obtained by incomplete combustion of paraffin wax candle, CS consists of superhydrophobic/superoleophilic carbon nanoparticles with size in the range 20–55 nm.[30] Although superhydrophobic, the network formed by CS nanoparticles is highly fragile and delicate since it involves weak van der Waals interactions between the nanoparticle agglomerates.[31] Thus, when deposited on a surface, the superhydrophobicity imparted by CS is temporary that can be easily washed away by, for example, water. To overcome this issue and maintain long term superhydrophobicity, research efforts have been made to improve the stability of CS that is deposited on metal meshes. For instance, Zhang *et al.*[32] prepared superhydrophobic stainless steel mesh by directly depositing CS *via* exposure to candle flame followed by immersion in a solution of polydimethylsiloxane (PDMS) and xylene. The resulting mesh exhibited a water contact angle of 156°, a roll-off angle of 3°, and an oil/water separation efficiency of 94%. The water contact angle was preserved when the mesh was subjected to multiple cycles of water jet impact test. This implied greater durability of the deposited CS due to the binding effect provided by PDMS. However, the use of hazardous xylene solvent is undesirable. Celik *et al.*[33] first collected CS by placing a beaker upside-down above a burning candle. The collected CS was then dispersed in a solution of carnauba wax and chloroform. Finally, the dispersion was spray-coated on a stainless-steel mesh to obtain a water contact angle of 172° and a roll-off angle of 3°. Also, oil/water separation efficiency of more than 90% was observed. The mesh was also able retain superhydrophobicity even after exposure to 400 cycles of continuous water spray with an impact pressure of 7.4 kPa. Although the durability was high, the collection of CS instead of direct deposition on the mesh is time consuming. This is because CS has a deposition rate of only 217 nm s^{-1}.[34] Also, the use of hazardous solvent for dissolving carnauba wax is a limitation. Song *et al.*[35] employed super glue as a binder for CS. In this study, CS was first collected on a silicon wafer followed by dispersion in ethanol. A stainless-steel mesh was immersed in a solution of super glue and ethanol. Following that, the mesh was immersed in the CS/ethanol dispersion to deposit the CS on the mesh. The resulting mesh produced a separation efficiency of more than 99.95% during 10 cycles of oil/water separation. However, superhydrophobicity was not realized and the mesh had a water contact angle of 146.8°. Although the aforementioned approaches have been successful in improving the stability of CS on metal meshes, further research efforts are still needed to fabricate superhydrophobic metal meshes that not only have a stable CS coating but also can be prepared using simple, inexpensive, and readily available materials.

Herein, we report a novel approach for preparing highly durable superhydrophobic copper mesh without using any harsh or expensive chemical agents. First, a copper mesh was coated with a thin layer of commercially available, low cost, and heat resistant RTV-1 silicone (1-part room-temperature-vulcanizing silicone) that acted as a binder. Next, the RTV-coated mesh was exposed directly to candle flame to deposit the carbon nanoparticles. In the final step, the superhydrophobicity was enhanced by creating surface micropatterns using femtosecond laser treatment. The benefit of using femtosecond laser is its ability to create spatially resolved hierarchal micro/nano surface features without requiring any chemical surface treatments. The development of micro/nano surface features is attributed to the specialized thermal and mechanical effects produced from ultrafast laser–matter interaction.[36–40] To the best of our knowledge, this is the first reported attempt that combines the superhydrophobicity imparted by CS nanoparticles and femtosecond laser treatment. Results showed that the laser-induced surface micropatterns were important not only in enhancing the water contact and roll-off angles, but also in imparting high durability to the mesh.

2. Experimental

2.1. Materials

Commercial copper wire mesh was used as a substrate (copper mesh 30, opening size: 542 microns) and was purchased from a local supplier. *n*-Hexane (ACS reagent, purity: >96.0%), acetone (ACS reagent, purity: ≥99.5%), and ethanol (absolute, purity: ≥99.8%) were purchased from Sigma-Aldrich (St. Louis, MO). Methylene blue powder was purchased from BDH Laboratory Supplies (Poole, England). All chemicals were used as received without further purification. Commercial high temperature RTV-1 silicone with temperature resistance up to 650 °F (brand: Galaxy, USA) and commercial paraffin wax candles were procured from the local market.

2.2. Fabrication of superhydrophobic mesh

The copper mesh was cut to a size of 30 mm × 30 mm and then cleaned with acetone prior to use. A thin layer of RTV-1 silicone was first applied to one side of the mesh in order to provide adhesion for the CS. To do this, the mesh was placed on a clean glass slide (washed with acetone) and a thin uniform layer of RTV-1 silicone was spread manually over the mesh surface. The mesh was then gently raised from the glass slide and the RTV-1 silicone-coated side of the mesh was immediately exposed to the paraffin wax candle flame to allow deposition of CS on the uncured RTV-1 silicone. The mesh was placed in the inner flame at approximately 1 cm from the wick of the candle. This is because, unlike the CS obtained from the flame tip, the CS deposited from the inner part of the flame is superhydrophobic and superoleophilic. It has been reported that CS particles from the inner flame of the candle form aggregates which are compact and contain higher amount of organics due to incomplete combustion of the wax vapor.[30,34] The flame tip was avoided since the CS obtained from the flame tip is hydrophilic and oleophilic due to complete combustion that results in more oxygen and ash contents. During the deposition of CS, the copper mesh was moved back and forth within the inner flame to obtain a uniform layer of CS. Also, the mesh was allowed to cool intermittently at room temperature for short periods of time in order to avoid excessive heating. The process of CS deposition was continued until the mesh turned black and was completely covered with CS. The CS-coated mesh was allowed to cool at room temperature. Following that, the mesh was ultrasonicated for 1 min in absolute ethanol using an ultrasonic bath (model: MH-020S digital ultrasonic cleaner, ultrasonic power: 120 W, frequency: 40 kHz, China) in order to remove the loosely bound CS particles. The mesh was finally allowed to dry before subjecting to femtosecond laser.

To create the surface micropatterns and achieve superhydrophobicity, a fiber-based femtosecond (fs) laser (AFSUFFL-300-2000-1030-300, Active Fiber Systems GmbH, Jena, Germany) was employed. The laser produced Gaussian pulses with a central wavelength of 1030 nm. The maximum power output, pulse duration, and pulse repetition rate were 300 W, 50 fs, and 50 kHz, respectively. The laser beam was focused and raster scanned on the mesh using a scan head. The focused spot diameter was around 50 μm. Laser structuring was performed in ambient air at a laser fluence of 0.76 J cm^{-2}, line spacing of 150 μm, and at a scan speed of 50 mm s^{-1}. The mesh was patterned with a crosshatch configuration. Laser was raster scanned over the mesh only once. After laser structuring, the

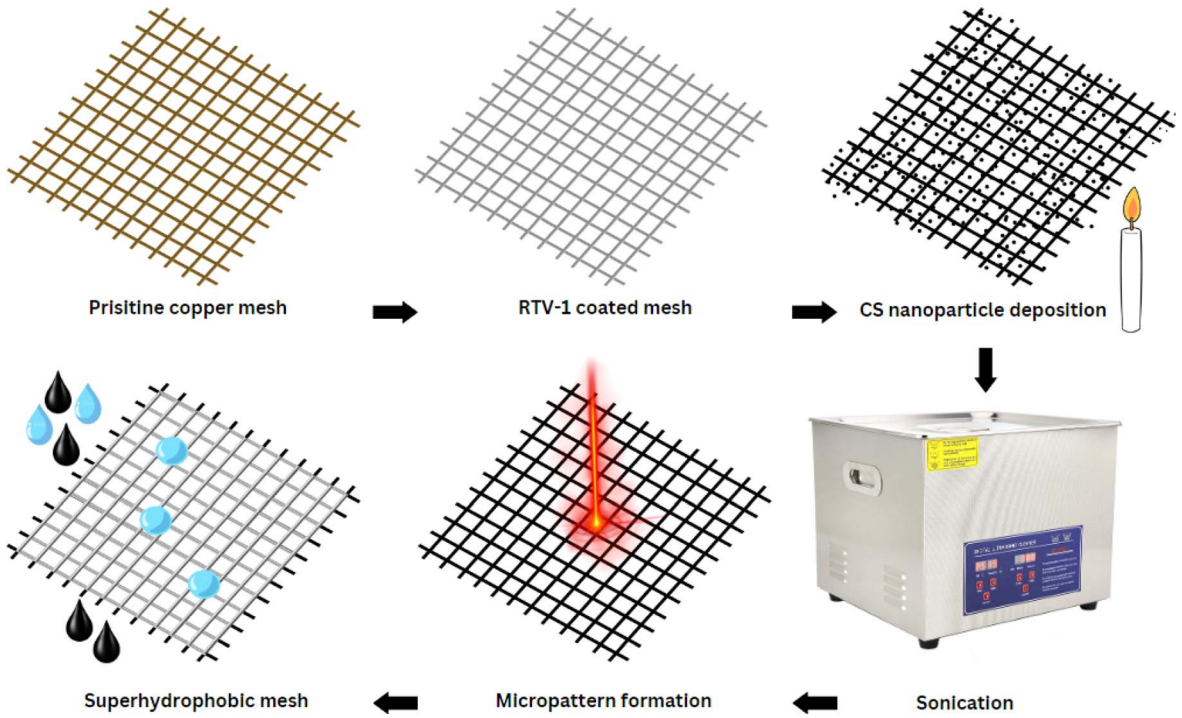

Fig. 1 Stepwise procedure for fabricating superhydrophobic mesh.

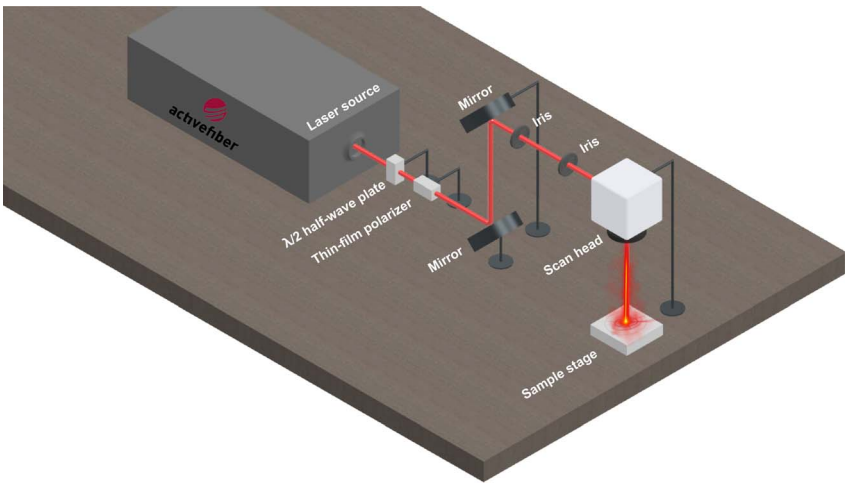

Fig. 2 Schematic diagram of the femtosecond laser setup for the formation of surface micropatterns.

obtained superhydrophobic mesh was employed for oil/water separation. The stepwise fabrication of the superhydrophobic mesh is depicted in Fig. 1 while the schematic diagram of the femtosecond laser system is shown in Fig. 2.

2.3. Characterizations

Surface morphology of the prepared superhydrophobic mesh was observed using a scanning electron microscope (SEM, VEGA 3 LMU, TESCAN, Czech Republic). The mesh sample was coated with gold/palladium prior to SEM imaging. The SEM was also equipped with a detector for energy dispersive X-ray spectroscopy (EDX, INCAx-act, Oxford Instruments) that was used to obtain the elemental compositions. Raman spectroscopy was performed using a Confocal Raman microscope (WITec, alpha 300R, Ulm, Germany) with an excitation laser wavelength of 532 nm. Attenuated total reflectance method for Fourier transform infrared spectroscopy (ATR-FTIR) was performed using an FTIR spectroscope (IRSpirit, Shimadzu, Kyoto, Japan). Measurements of water contact and roll-off angles were performed at ambient conditions using a drop shape analyzer (DSA100M, Kruss GmbH, Hamburg, Germany).

2.4. Durability tests

The prepared superhydrophobic mesh was subjected to a water jet in order to assess its durability. To do this, the mesh was placed in a laboratory wash sink and the vertical distance between the water outlet from the tap and the surface of the mesh was maintained at 10 cm. The diameter (d) of the water tap outlet was 1.8 cm and the average water flow rate (Q) from the tap was measured to be 52 mL s^{-1}. The resulting impact velocity ($v = 4Q/\pi d^2$) was, therefore, approximately 20 cm s^{-1}. After being subjected to the water jet, the mesh was dried using a hot air blower. The water contact and roll-off angles were then measured using the drop shape analyzer. The water jet durability test was repeated multiple times. Also, durability was assessed *via* tape-peeling test. For this, a piece of scotch tape (Scotch® Magic™ tape 810, 3M, St. Paul, MN) was applied on top of the mesh. A 200 g weight was then placed on top to allow good contact between the tape and the mesh. The tape was then peeled off after which the water contact and roll-off angles were measured using the drop shape analyzer. All durability test runs were performed at ambient conditions.

2.5. Oil/water separation tests

Oil/water separation experiments were carried out using a custom-built separator apparatus that allowed for gravity-driven separation of oil/water mixtures. The vertical separator, shown in Fig. 3, consisted of two cylindrical plastic tubes that were connected with a threaded PVC union at the center. The mesh was placed inside the union with the superhydrophobic side facing upwards. An O-ring was also placed with the mesh to

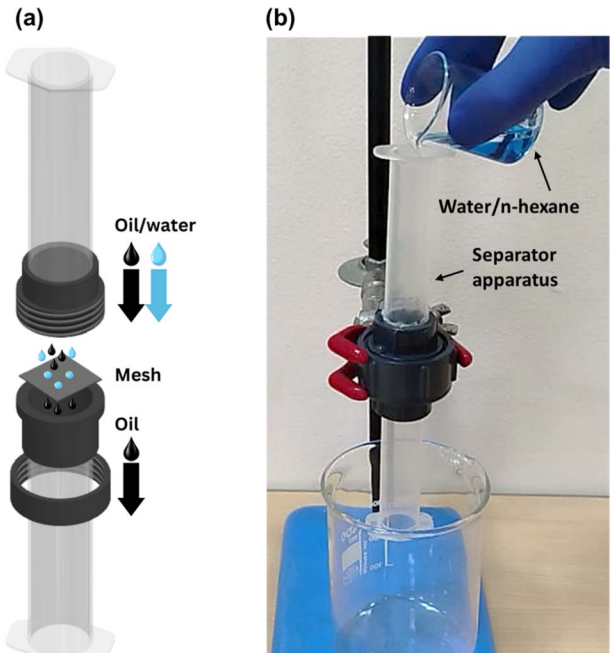

Fig. 3 (a) Exploded-view diagram and (b) actual photograph of the gravity-driven oil/water separator column employed in this study.

avoid any leakage from the union. The cross-sectional area (A) of the mesh available for oil permeation was equal to 2.54 cm^2. The separator was mounted on an iron stand. Oil/water mixtures were prepared by adding n-hexane to distilled water (dyed with methylene blue). The volume of each phase was 5 mL (1 : 1 ratio). To perform oil/water separation, the immiscible mixture of n-hexane/water was added slowly from the top of the separator. The superhydrophobic mesh allowed n-hexane to permeate through while the water accumulated on top of the mesh. The volumes of both n-hexane and water after the separation were recorded using a graduated cylinder. The separation efficiency (η) was calculated as follows:[41]

$$\eta = \frac{V_1}{V_0} \times 100\% \quad (1)$$

where, V_0 and V_1 represent the volume of water before and after the separation.

The flux of oil (J) permeating through the mesh was calculated as follows:[41]

$$J = \frac{V}{A \times t} \times 100\% \quad (2)$$

where, V is the volume of the permeate, A is the cross-sectional area of the mesh available for separation, and t is the time taken for the separation. The oil/water separation experiments were conducted multiple times using the same mesh in order to assess the durability. All oil/water separation experiments were carried out at ambient conditions.

3. Results & discussions

3.1. Surface morphology and chemical composition analysis

Surface morphology, in general, plays a significant role in the endowment of superhydrophobic characteristics to different surfaces. To impart superhydrophobicity, the surface morphology can be modified to create micro/nanostructures and roughness features on the surface. In this work, low-cost CS nanoparticles were first deposited on a copper mesh after covering it with a thin layer of RTV-1 silicone. The RTV-1 was employed to allow for adhesion of CS nanoparticles on top of the mesh. Fig. 4 shows the SEM images of the mesh with CS nanoparticles adhered to the surface using RTV-1 binder. The mesh is denoted as RTV + CS hereafter. These images were taken prior to femtosecond laser structuring on the mesh surface. It can be seen from Fig. 4(a) that the CS nanoparticles on the mesh surface were well-distributed and resulted in the formation of roughness features. The presence of CS

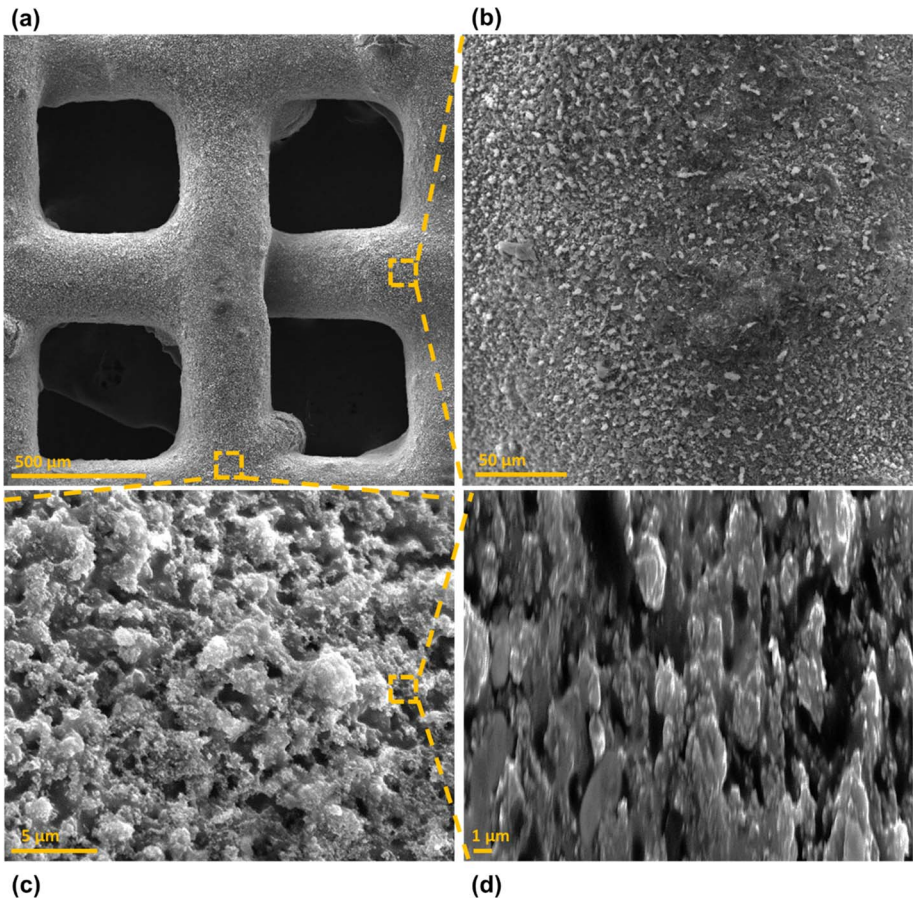

Fig. 4 (a) SEM image of copper mesh coated with CS using RTV-1 as binder (RTV + CS), (b) is a zoomed in view of the segment highlighted in (a), (c) is a zoomed in view of the segment highlighted in (a), and (d) is a zoomed in view of the segment highlighted in (c). Images taken prior to femtosecond laser structuring.

nanoparticles can be seen with more clarity in the zoomed in view in Fig. 4(b)–(d). It can be seen that the CS nanoparticles existed as irregular agglomerates and imparted roughness to the mesh surface. Overall, the RTV-1 bonded the CS nanoparticles on top of the mesh and the presence of CS nanoparticles effectively created roughness features that were important for achieving high hydrophobicity.

Fig. 5 shows the elemental compositions, obtained by EDS analysis, for the RTV + CS mesh prior to femtosecond laser structuring. As evident from the elemental compositions in Fig. 5(b), the content of C on the mesh was the highest (47.3 wt%). The C content was due to the deposited CS nanoparticles in addition to the C from the polysiloxane fraction of RTV-1. The elemental analysis also showed the presence of Si, O, and Ca elements, which were originally present within the components of RTV-1. The presence of both Si and O was due to the polysiloxane fraction of RTV-1. The element Ca, on the other hand, was due to the presence of calcium carbonate in RTV-1 which is typically added as a non-reinforcing filler.[42] Fig. 5(c) shows the EDS elemental mapping of the zoomed in view of the segment highlighted in Fig. 5(a). The identified elements and their compositions in Fig. 5(d) were found to be almost the same as in Fig. 5(a). This indicated that the RTV-1 binder layer and the CS nanoparticle deposition was uniform on the mesh surface without significant spatial variations in the elemental compositions.

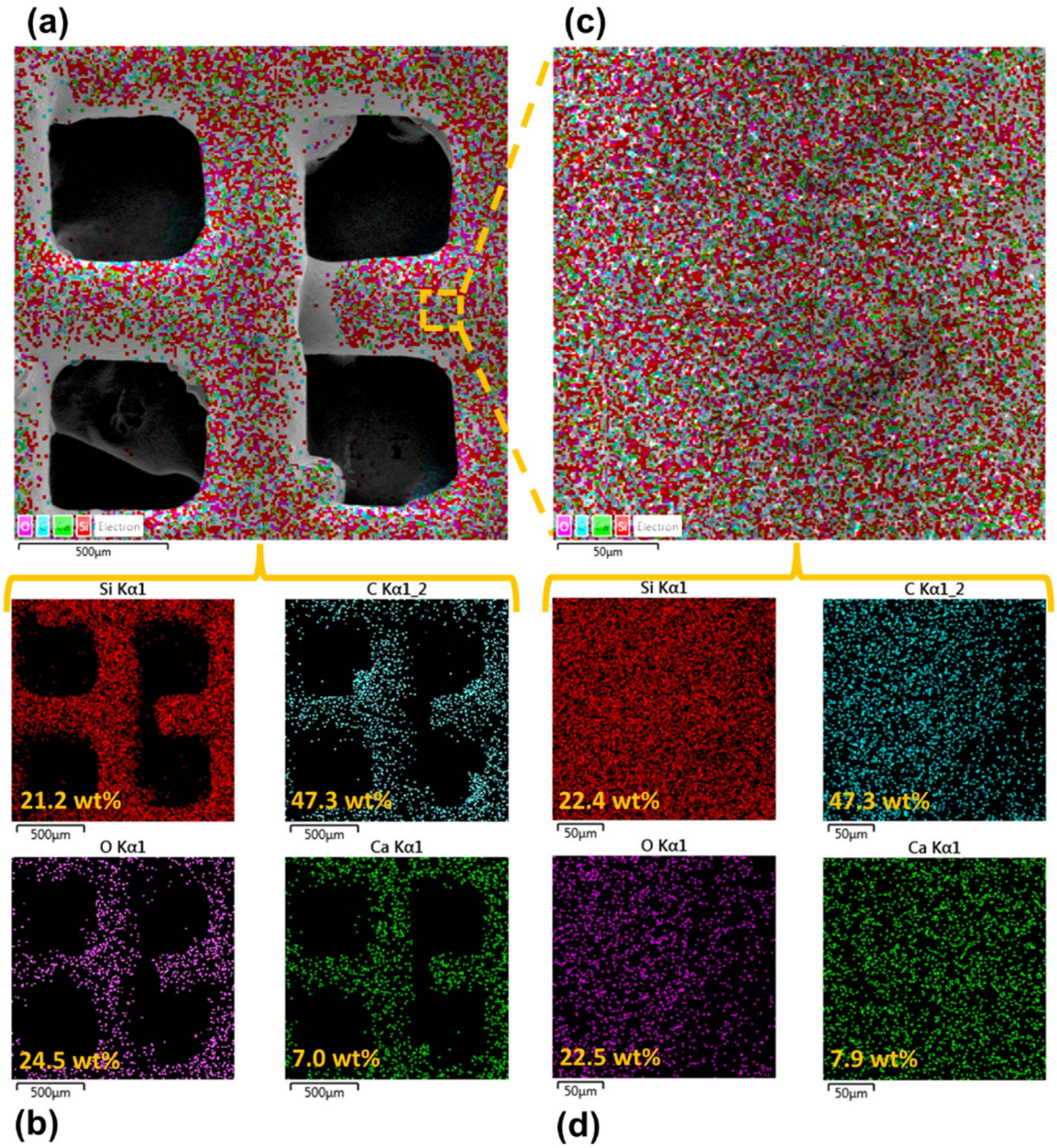

Fig. 5 (a) Elemental layered image and (b) elemental compositions of the RTV + CS mesh, (c) elemental layered image and (d) elemental compositions for the zoomed in view of the segment highlighted in (a). EDS analysis performed prior to femtosecond laser structuring.

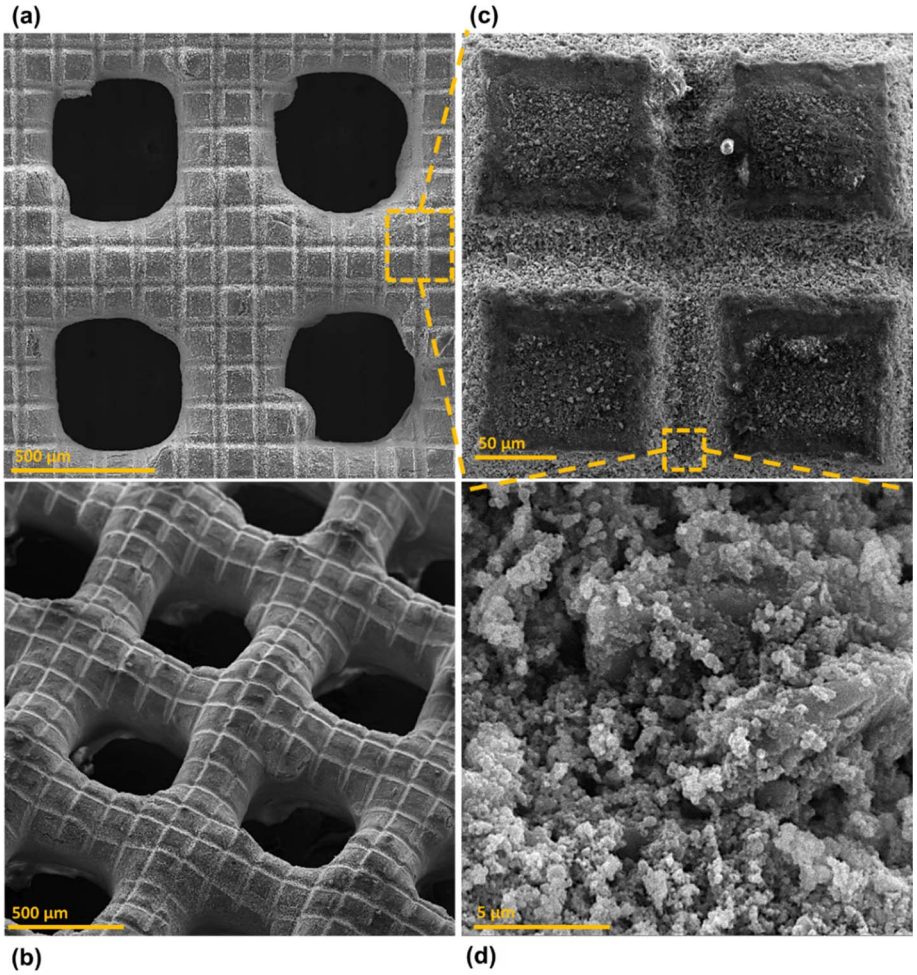

Fig. 6 SEM image of femtosecond laser structured copper mesh coated with CS using RTV-1 as binder (RTV + CS + LS) with plane (a) parallel and (b) tilted 40° relative to the sample stage. (c) is a zoomed in view of the segment highlighted in (a), and (d) is a zoomed in view of the segment highlighted in (c).

Fig. 6 shows the morphology of the mesh after creating the surface micropatterns using femtosecond laser. Structuring was performed in ambient air at a laser fluence of 0.76 J cm^{-2}, line spacing of 150 μm, and at a scan speed of 50 mm s^{-1}. This mesh is referred to as RTV + CS + LS hereafter, where LS indicates laser structuring. Since the mesh was patterned with a cross-hatch configuration during laser structuring, horizontal and vertical laser ablated zones were created resulting in the formation of square array patterns on the mesh surface, as shown in Fig. 6(c). The horizontal and vertical laser ablated zones were in direct contact with the laser and the ablation effects within these zones produced several particles at the micro, sub-micro, and nano levels. These are shown in the zoomed in image of the laser ablated zone in Fig. 6(d). The square patterns, on the other hand, were zones on the mesh which were not in direct contact with the laser during the ablation. These patterns were at the microlevel with submicron particles decorated on the top. The submicron decorations can be attributed to the molten material ejected during laser ablation that deposited on top of the square micropatterns. Thus, hierarchical surface structural features were produced by femtosecond laser structuring. These hierarchical surface structures play an important role in creating multilevel micro and nanoscale roughness features and, consequently, imparting superhydrophobic characteristics to the mesh.

The elemental compositions for the RTV + CS + LS mesh are shown in Fig. 7. From the elemental layered image in Fig. 7(a) and the elemental compositions in Fig. 7(b), it can be seen that, overall, the O content on the mesh increased to 39.3 wt% after femtosecond laser structuring. This can be attributed to the formation of laser-induced oxides such as SiO_2 (ref. 43) due to the partial decomposition of the polysiloxane fraction in RTV-1. In addition, the overall content of C decreased to 23.9 wt% after femtosecond laser structuring compared to 47.3 wt% C on the unstructured mesh. This can be attributed to the loss of CS nanoparticles on the mesh surface during laser ablation. The generation of plasma plume during ablation can result in some CS nanoparticles to debond from the RTV-1 binder and escape from the mesh surface. As a result, the recorded content of C was lower compared to the unstructured mesh. Fig. 7(c) and (d)

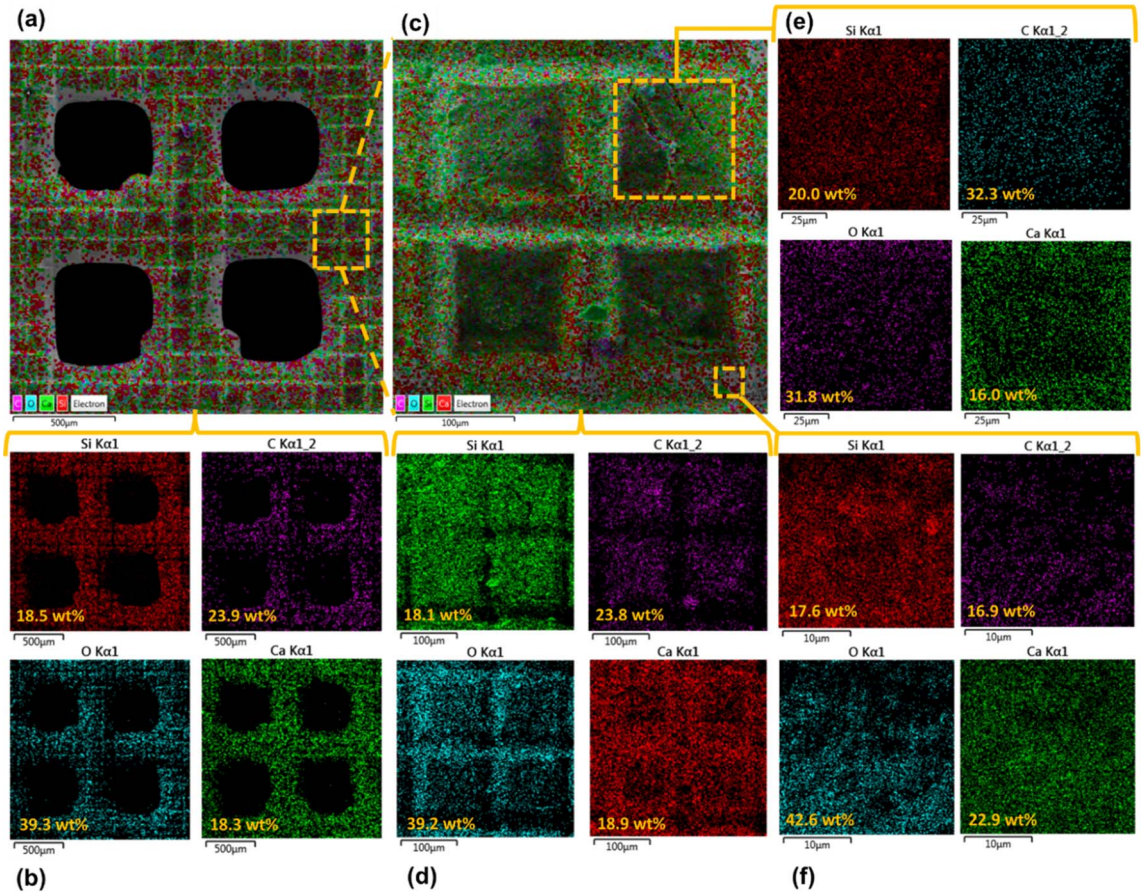

Fig. 7 (a) Elemental layered image and (b) elemental compositions of the RTV + CS + LS mesh, (c) elemental layered image and (d) elemental compositions for the zoomed in view of the segment highlighted in (a), (e) elemental compositions for the unablated area highlighted in (c), and (f) elemental compositions for the ablated area highlighted in (c).

show the elemental layered image and the EDS elemental mapping, respectively, for the zoomed in view of the segment highlighted in Fig. 7(a). Again, the identified elements and their compositions were found to be almost the same as in Fig. 7(b). This indicated that the performed laser structuring was uniform on the mesh surface and did not result in any significant spatial variations of the elemental compositions. Fig. 7(e) shows the elemental compositions for the unablated square pattern highlighted in Fig. 7(c). It can be seen that, compared to the values in Fig. 7(b), the content of C on the square pattern was higher (32.3 wt%) while the O content was lower (31.8 wt%). This was due to the fact that square patterns were not directly exposed to the laser during structuring and hence, the loss of CS nanoparticles and the decomposition of the polysiloxane fraction to SiO_2 was not significant. These findings were further supported by the elemental compositions in Fig. 7(f) for the ablated region shown in Fig. 7(c). Within the ablated region, the C content was much lower while the O content was much higher. Thus, for these regions, the loss of CS nanoparticles and the decomposition of the polysiloxane fraction to SiO_2 was much higher due to direct contact with the laser during ablation.

Further chemical analysis for the mesh was conducted using FTIR spectroscopy wherein the surface functional groups and chemical bonds were identified. Fig. 8 shows FTIR spectra for the mesh before and after femtosecond laser structuring. It can be observed that the major peaks related to RTV-1 and CS in the FTIR spectra remained the same before and after laser

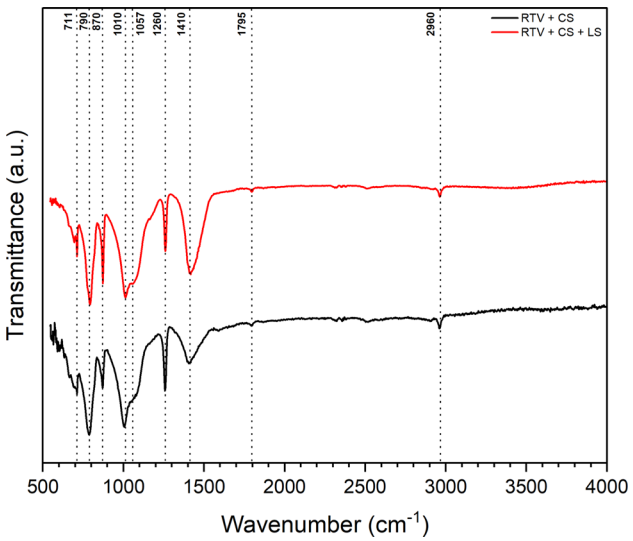

Fig. 8 FTIR spectra for the meshes RTV + CS and RTV + CS + LS.

structuring. In case of CS, it has been reported that, generally, the (C–H) band stretching occurs between 3300 and 2800 cm^{-1}.[31,44] Thus, the peak at 2960 cm^{-1} indicated aliphatic (C–H) band stretching. Also, the carbonyl (C=O) stretching bands occur between 1800 to 1650 cm^{-1}.[31,44] This is indicated by the peak at 1795 cm^{-1} in Fig. 8 that shows the presence of carbonyl (C=O) group in the CS deposited on the mesh. The peak at 1410 cm^{-1} indicated (C–H) stretching vibration which corresponded to $-CH_2$ functional group while at 1260 cm^{-1}, the C–H antisymmetric deformation of C=C band was highlighted. The peaks between 1040 and 1240 cm^{-1} generally indicate (C–O) bonds of ethers, carboxylic acids, and polysaccharide.[31] Thus, in Fig. 8, the peak at 1057 cm^{-1} corresponded to the carboxyl group stretching of oxidized carbons.[44] Also, the peak at 870 cm^{-1} was associated with the presence of substituted aromatic C–H group.[31] Overall, the FTIR peaks for the CS deposited on the mesh agreed with the literature reported peak values.[31,44] Also, the peaks for CS were the same before and after femtosecond laser structuring indicating that CS was not completely removed during the laser ablation process. In general, the network formed by CS nanoparticles is highly fragile and delicate since it only involves weak van der Waals interactions between the nanoparticle agglomerates. In the absence of the binder, the CS on the mesh surface would simply be ejected and leave the surface under the strong action of the laser plasma plume. However, for the RTV + CS + LS mesh, CS was still present on the surface, predominantly, within the unablated square patterns. Besides CS, the FTIR spectra showed the characteristic peaks for the RTV-1 binder. The peak at 2960 cm^{-1} can also correspond to the $-CH_3$ asymmetric stretch in RTV-1.[45,46] Also, RTV-1 shows a peak for $Si–CH_3$ between 1240 and 1280 cm^{-1}.[45] Thus, the peak at 1260 cm^{-1} can also possibly represent $Si–CH_3$ bond in RTV-1. Also, the peaks at 1010, 790, and 711 cm^{-1} corresponded to Si–O–Si, $Si(CH_3)_2$, and $Si(CH_3)_3$ in RTV-1, respectively.[45]

Similar observations were made from the Raman spectra of the mesh before and after femtosecond laser structuring shown in Fig. 9. The presence of CS on the mesh was confirmed in both cases. Again, this indicated that CS was not completely removed during the laser ablation process. The Raman spectra showed two distinct peaks related to CS. The first peak at 1348 cm^{-1} corresponded to the disordered graphitic phase (D band) and represented amorphous carbon. The second peak at 1570 cm^{-1} was the G band that corresponded to the E_{2g} mode of graphite due to the vibration of sp^2-bonded carbon atoms in a 2D hexagonal lattice.[47,48] The remaining peaks identified in Fig. 9 correspond to the RTV-1 binder. The peaks at 437, 670, 899, 1238, and 1411 cm^{-1} are attributed to Si–O–Si symmetric stretch, $Si–CH_3$ symmetric rocking, $-CH_3$ asymmetric rocking, $-CH_3$ symmetric bending/Si–O–Si asymmetric stretch, and $-CH_3$ asymmetric bending, respectively.[46,49]

3.2. Wettability analysis

In this study, femtosecond laser structuring played a critical role in achieving high water contact angle and low roll-off angle for the prepared mesh. As shown in Fig. 10, after creation of surface micropatterns, the resulting RTV + CS + LS mesh was superhydrophobic and exhibited a very high water contact angle of 168.9° and a low roll-off angle of only 5.9°. Thus, the criteria for superhydrophobicity, *i.e.* water contact angle higher than 150° and roll-off angle less than 10°, was satisfied. The synergistic effect of CS and laser-induced micropatterns in achieving superhydrophobicity was verified by measuring the water contact and roll-off angles of the mesh in the absence of CS, femtosecond laser structuring, or both. The water contact and roll-off angles are compared in Fig. 10. When the mesh was prepared by only coating RTV-1 and allowed to cure at room temperature, the water contact angle of the resulting mesh (named as RTV-only mesh) was 128.2°. Although slightly hydrophobic, the mesh with only RTV-1 coating was not able to satisfy the superhydrophobicity criteria. The slight hydrophobicity observed was due to the intrinsic hydrophobicity of RTV-1 due to its low surface energy and the low polarity of the constituent silicone polymer chains.[50] Also, the roll-off angle

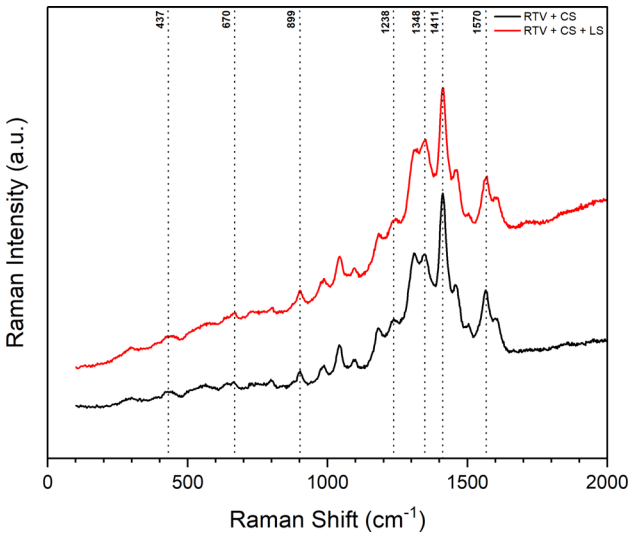

Fig. 9 Raman spectra for the meshes RTV + CS and RTV + CS + LS.

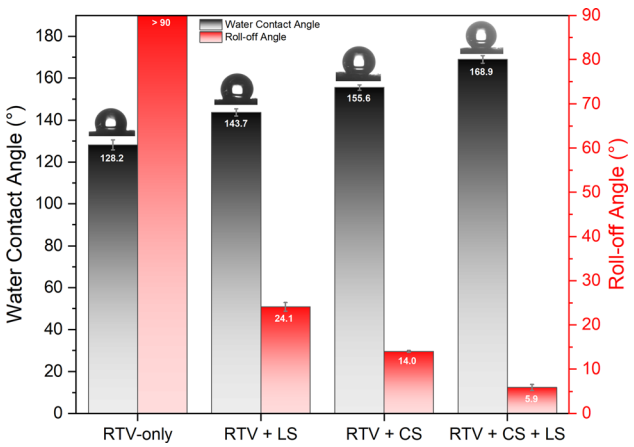

Fig. 10 Water contact angles and roll-off angles for the meshes with different surface coatings.

was more than 90° since the water drop on the mesh surface was not able to roll-off even at an angle of 90°. Next, the mesh coated with RTV-1 alone was structured using femtosecond laser (referred to as RTV + LS mesh). Structuring was performed in ambient air at a laser fluence of 0.76 J cm^{-2}, line spacing of 150 μm, and at a scan speed of 50 mm s^{-1}. The improvement in the hydrophobicity was evident upon femtosecond laser structuring since the water contact angle increased to 143.7° and the roll-off angle decreased to 24.1°. This can be attributed to the ability of femtosecond laser to create micro/nano roughness features on the mesh surface. Although femtosecond laser structuring enhanced the hydrophobicity, the mesh in this case was also not superhydrophobic.

In case of mesh coated with CS on top of RTV-1 binder (RTV + CS), the water contact and roll-off angles were 155.6° and 14.0°, respectively. Comparing with the RTV-only mesh, the presence of CS nanoparticles resulted in a significant enhancement of the hydrophobicity. The CS nanoparticles were deposited on the mesh from the inner flame of the candle. These nanoparticles are reported to be compact and contain high content of organics due to the incomplete combustion of the wax vapor. As a result, the CS nanoparticles from the inner flame are superhydrophobic and superoleophilic.[30] Due to the excellent hydrophobicity of the CS nanoparticles, the RTV + CS mesh exhibited much higher water contact angle compared to the RTV-only mesh. Also, with the presence of CS nanoparticles, the observed roll-off angle was only 14.0°. However, the water repellence of this mesh was still inferior to the RTV + CS + LS mesh, *i.e.*, the one prepared with femtosecond laser structuring. The combined effect of CS nanoparticles and the laser-induced hierarchical surface structures and multilevel micro and nanoscale roughness features produced the best results. Thus, the best water repellence was observed for the RTV + CS + LS mesh which was fabricated by performing femtosecond laser structuring on the mesh coated with CS on top of the RTV-1 binder. The superhydrophobicity of the RTV + CS + LS mesh is demonstrated in Video S1 – ESI.† It should be noted that the water contact and roll-off angles were measured using a drop volume of 10 μL or higher. This is because water drops of lesser volumes were unable to adhere to the surface of the superhydrophobic RTV + CS + LS mesh. As depicted in Fig. 11 and shown in Video S2 – ESI,† a 5 μL water drop was unable to adhere to the surface of RTV + CS + LS mesh even after pressing it hard on the surface. This was due to the superhydrophobic characteristics that resulted in a very low water adhesion force. Besides being superhydrophobic, CS are superoleophilic[30] and, as a result, the RTV + CS + LS mesh was superoleophilic and easily allowed *n*-hexane drops to pass through when using the drop shape analyzer.

3.3. Durability evaluation

The durability of the RTV + CS + LS mesh was evaluated by performing water jet impact test. The test was performed with a water jet impact velocity of approximately 20 cm s^{-1}. After each cycle of the water jet impact test, the mesh was dried, and the water contact and roll-off angles were measured. Fig. 12 shows the measured water contact and roll-off angles after each cycle of water jet impact test. It can be seen that the superhydrophobicity of the mesh was maintained even after impacting it 50 times with the water jet. At the end of 50 cycles of the durability test, the water contact angle showed a negligible decline. The water contact angle measured at the end of 50 cycles was 168.6° compared to the initial value of 168.9°. Similarly, the roll-off angle was also preserved after subjecting to 50 cycles of the water jet impact test. The initial roll-off angle was 5.9° while at the end of 50 cycles, the measured roll-off angle was 6.0°.

The RTV + CS + LS mesh also exhibited good durability during tape-peeling test (Fig. 13). After five cycles of tape-peeling, the water contact angle was 166.6°, implying very minor change upon tape-peeling. The roll-off angle, on the other hand, increased by 4° to 9.9°. Thus, the RTV + CS + LS

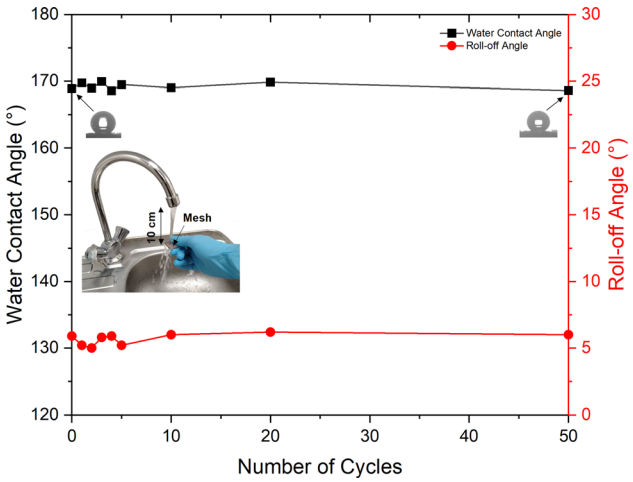

Fig. 12 Water contact and roll-off angles for the RTV + CS + LS superhydrophobic mesh after several cycles of water jet durability test.

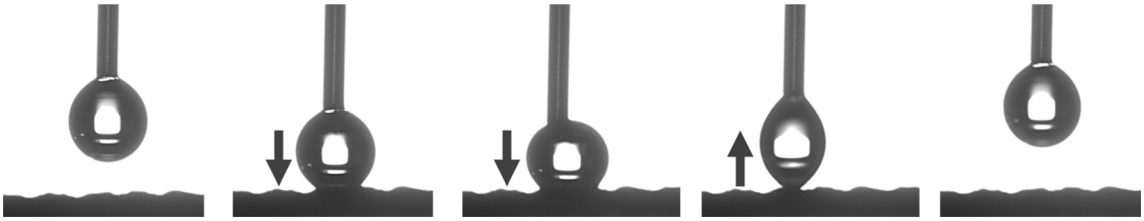

Fig. 11 Schematic showing no adhesion of 5 μL water drop on the surface of RTV + CS + LS mesh.

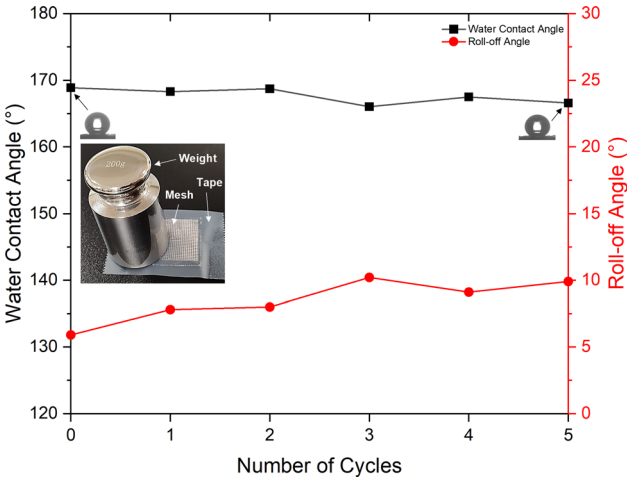

Fig. 13 Water contact and roll-off angles for the RTV + CS + LS superhydrophobic mesh after several cycles of tape-peeling test.

mesh was able to retain its superhydrophobicity after the tape-peeling test. The consistently stable values of water contact and roll-off angles indicated high mechanical durability of the RTV + CS + LS mesh in which the adhesion of RTV-1 with the copper mesh, the adhesion of CS nanoparticles with RTV-1, and the micro/nano roughness features created by femtosecond laser structuring were not affected by the water jet and tape-peeling. In case of RTV + CS mesh, the observed mechanical durability was inferior compared to the RTV + CS + LS mesh. After five cycles of tape-peeling, the water contact angle of the RTV + CS mesh declined to 149.6° (a decline of 6° compared to a decline of only 2.3° for the RTV + CS + LS mesh). The roll-off angle of the RTV + CS mesh declined significantly to a value of 27.2° (a decline of 13.2° compared to the initial value). The results of the durability tests highlight the significant contributions of the femtosecond laser structuring in imparting superhydrophobic characteristics to the mesh. With laser structuring, the RTV + CS + LS mesh not only showed enhancements in the water contact and roll-off angles, but also exhibited increased mechanical durability. This suggests that the laser-induced micro/nano structural features were durable and the CS nanoparticles in the RTV + CS + LS mesh were more strongly embedded within the RTV-1 binder. Laser-matter interaction, in general, is known to produce specialized thermal and mechanical effects including melting, vaporization, and re-solidification. During laser structuring, the melting and vaporization of RTV-1 with subsequent re-solidification may have provided strong anchoring effect for the CS nanoparticles, thereby, imparting higher mechanical durability to the RTV + CS + LS mesh.

3.4. Oil/water separation performance

The oil/water separation performance of RTV + CS + LS mesh was evaluated by separating a mixture of *n*-hexane and water under gravity. The water layer was dyed with methylene blue to help differentiate it from the *n*-hexane layer. The mesh was placed inside a vertical separator with its superhydrophobic side facing up. The *n*-hexane/water mixture was then added from the top of the separator to begin the separation process. Due to the superhydrophobic and superoleophilic behavior of the RTV + CS + LS mesh, *n*-hexane was able to easily permeate through it while water started to accumulate on top of the superhydrophobic surface of the mesh. The separation of *n*-hexane and water is demonstrated in Video S3 – ESI.† When performed for the first time, the *n*-hexane/water separation efficiency was found to be 96%. To assess the durability of the mesh, the same mesh was employed 10 times to separate different batches of *n*-hexane/water mixture. Fig. 14 shows the separation efficiency of the mesh for each of the 10 separation cycles. During these cycles, the average flux of *n*-hexane permeating through the RTV + CS + LS mesh was 8860 L m^{-2} h^{-1}. It can be seen that the RTV + CS + LS mesh was able to consistently maintain a high separation efficiency without any significant decline in the separation performance. This behavior was not observed in case of RTV + CS mesh. As depicted in Fig. 13, the oil/water separation efficiency of the RTV + CS mesh declined significantly upon repeated use. The observed separation efficiency was high at the beginning and measured to be 90% during the first cycle. The mesh only produced reasonably high separation efficiency only up to the fourth cycle. After the sixth cycle, the separation efficiency of the RTV + CS mesh was only 50%. Beyond that, the RTV + CS mesh was unable to separate the *n*-hexane/water mixture. Thus, in case of RTV + CS mesh, *n*-hexane was able to wash away the CS nanoparticles upon repeated exposure. This again highlights the importance of femtosecond laser structuring in imparting stable superhydrophobic characteristics to the mesh. The presence of laser-induced micro/nano structural features and the strong anchoring of the CS nanoparticles resulted in higher durability and allowed for repeated use of the RTV + CS + LS mesh. Table 1 compares the RTV + CS + LS mesh with previously reported CS-based and other oil/water separation materials. Comparisons have been made based on the separation

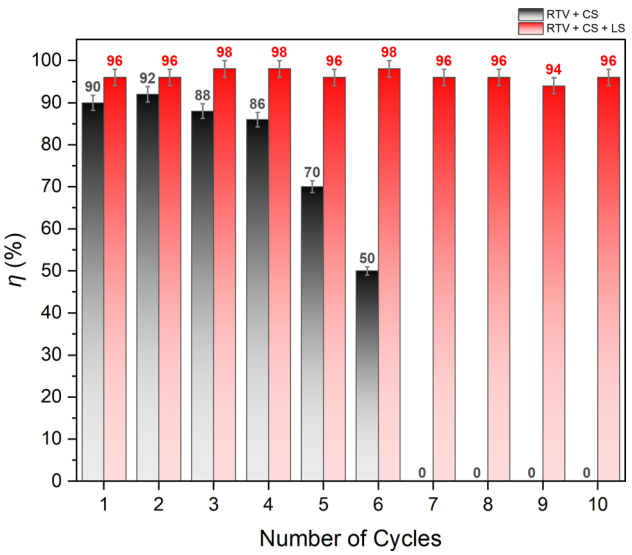

Fig. 14 Oil/water separation performance of RTV + CS and RTV + CS + LS meshes.

Table 1 Comparison of RTV + CS + LS mesh with previously reported CS-based and other oil/water separation materials

Material details	Water contact angle (roll-off angle)	Separation performance	Comments on durability	Reference
CS deposited on PDMS-coated stainless-steel mesh	156° (3°)	η: 94%	Stable wettability against multiple cycles of tape-peeling and water jet impact tests	32
CS deposited on glue-coated stainless-steel mesh	146.8°	η: >99.95%	Superhydrophobicity retained after 20 separation cycles	35
CS deposited on roughened copper mesh	153° (<5°)	η: 95%, J: 4378 L m^{-2} h^{-1}	Slight decline in separation efficiency upon repeated use	51
CS-polydimethylsiloxane (PDMS) deposited on stainless-steel mesh *via* dip coating	162° (4°)	η: >98%, J: 7810 L m^{-2} h^{-1}	Separation efficiency remained >98% after 15 cycles of separation, superhydrophobicity retained after 5 tape-peeling cycles	52
CS and silica deposited on stainless-steel mesh	160° (5°)	η: >99%	Separation efficiency remained >98% after 55 cycles of separation	53
CS and silica nanoparticles deposited on polyurethane foam *via* dip coating	155° (7°)	η: >99%	Stable separation efficiency upon repeated use	54
Polystyrene (PS) and octadecyltrichlorosilane (OTS) coated on stainless-steel mesh through dip-coating	157.5° (6°)	η: >97%, J: 1689.2 L m^{-2} h^{-1}	Superhydrophobicity retained after 20 cycles of tape-peeling test	55
PS-silica coated stainless steel mesh	158.5° (5°)	η: >99.93%	Superhydrophobicity retained after 25 cycles of tape-peeling test	56
Fluoropolymer coated stainless-steel mesh prepared by chemical vapor deposition	170°	η: >99%	—	57
Stainless-steel mesh coated using electrodeposition ($ZnCl_2$ and lauric acid) and electrophoresis (α-Al_2O_3)	170° (1°)	η: >99%	Slight increase in roll-off angle and almost stable water contact angle with 10 cycles of tape-peeling test	58
RTV + CS + LS copper mesh	168.9° (5.9°)	η: >98%, J: 8860 L m^{-2} h^{-1}	Stable performance during 10 separation cycles, 5 tape-peeling cycles, and 50 water jet impact cycles	This work

efficiency and the durability tests highlighted in this study. The comparison shows that the wettability and durability of RTV + CS + LS mesh is either superior or comparable to the other oil/water separation materials reported in the literature. The observed robustness of the RTV + CS + LS mesh signifies its possible utilization in practical oil/water separation applications where long-term operation and repeated use are highly important.

4. Conclusions

A superhydrophobic mesh was prepared by first depositing low-cost carbon nanoparticles on a copper mesh using RTV-1 as a binder. Micropatterns were then created on the mesh surface using femtosecond laser. By creating the surface micropatterns with embedded carbon nanoparticles, fabrication of a superhydrophobic mesh with high water contact angle and low roll-off angle was made possible. The mesh proved to be exceptionally efficient in separating *n*-hexane/water mixtures with the aid of gravity. Furthermore, it demonstrated remarkable durability, maintaining its superhydrophobic properties even after tape-peeling and enduring repeated impacts from a water jet. Additionally, the mesh consistently exhibited stable separation efficiency across many cycles of *n*-hexane/water separation tests. The manufactured mesh emerges as a robust solution suitable for real-world oil/water separation applications that demand prolonged operation and repeated utilization. The surface micropatterns step played a pivotal role in the fabrication process without which the mesh displayed reduced durability and could not maintain stable oil/water separation performance over multiple cycles.

Data availability

Data underlying the results presented in this paper are not publicly available at this time but may be obtained from the authors upon reasonable request.

Author contributions

Muhammad Qasim: investigation, data curation, visualization, methodology, writing – original draft, review and editing. Asghar Ali: investigation, methodology, A. S. Alnaser: conceptualization, methodology, validation, supervision, project administration, review and editing.

Conflicts of interest

The authors declare that they have no known competing financial interests or personal relationships that could have appeared to influence the work reported in this paper.

Acknowledgements

We acknowledge support from the American University of Sharjah through the FRG23-C-S56 Grant.

References

1 S. Rasouli, N. Rezaei, H. Hamedi, S. Zendehboudi and X. Duan, Superhydrophobic and superoleophilic membranes for oil-water separation application: A comprehensive review, *Mater. Des.*, 2021, **204**, 109599, DOI: 10.1016/j.matdes.2021.109599.

2 I. M. Cozzarelli, K. J. Skalak, D. B. Kent, M. A. Engle, A. Benthem, A. C. Mumford, K. Haase, A. Farag, D. Harper, S. C. Nagel, L. R. Iwanowicz, W. H. Orem, D. M. Akob, J. B. Jaeschke, J. Galloway, M. Kohler, D. L. Stoliker and G. D. Jolly, Environmental signatures and effects of an oil and gas wastewater spill in the Williston Basin, North Dakota, *Sci. Total Environ.*, 2017, **579**, 1781–1793, DOI: 10.1016/j.scitotenv.2016.11.157.

3 J. Neff, K. Lee and E. M. DeBlois, Produced Water: Overview of Composition, Fates, and Effects, in *Produced Water: Environmental Risks and Advances in Mitigation Technologies*, ed. K. Lee and J. Neff, Springer New York, New York, NY, 2011, pp. 3–54, DOI: 10.1007/978-1-4614-0046-2_1.

4 J. Beyer, A. Goksøyr, D. Ø. Hjermann and J. Klungsøyr, Environmental effects of offshore produced water discharges: A review focused on the Norwegian continental shelf, *Mar. Environ. Res.*, 2020, **162**, 105155, DOI: 10.1016/j.marenvres.2020.105155.

5 J. Beyer, H. C. Trannum, T. Bakke, P. V. Hodson and T. K. Collier, Environmental effects of the Deepwater Horizon oil spill: A review, *Mar. Pollut. Bull.*, 2016, **110**, 28–51, DOI: 10.1016/j.marpolbul.2016.06.027.

6 X. Yue, Z. Li, T. Zhang, D. Yang and F. Qiu, Design and fabrication of superwetting fiber-based membranes for oil/water separation applications, *Chem. Eng. J.*, 2019, **364**, 292–309, DOI: 10.1016/j.cej.2019.01.149.

7 M. A. D'Andrea and G. K. Reddy, The Development of Long-Term Adverse Health Effects in Oil Spill Cleanup Workers of the Deepwater Horizon Offshore Drilling Rig Disaster, *Front. Public Health*, 2018, **6**, 117, DOI: 10.3389/fpubh.2018.00117.

8 S. Rasouli, N. Rezaei, H. Hamedi, S. Zendehboudi and X. Duan, Superhydrophobic and superoleophilic membranes for oil-water separation application: A comprehensive review, *Mater. Des.*, 2021, **204**, 109599, DOI: 10.1016/j.matdes.2021.109599.

9 V. Singh, Y.-J. Sheng and H.-K. Tsao, Facile fabrication of superhydrophobic copper mesh for oil/water separation and theoretical principle for separation design, *J. Taiwan Inst. Chem. Eng.*, 2018, **87**, 150–157, DOI: 10.1016/j.jtice.2018.03.025.

10 C. Chen, D. Weng, A. Mahmood, S. Chen and J. Wang, Separation Mechanism and Construction of Surfaces with Special Wettability for Oil/Water Separation, *ACS Appl. Mater. Interfaces*, 2019, **11**, 11006–11027, DOI: 10.1021/acsami.9b01293.

11 J. Gong, B. Xiang, Y. Sun and J. Li, Janus smart materials with asymmetrical wettability for on-demand oil/water separation: a comprehensive review, *J. Mater. Chem. A*, 2023, **11**, 25093–25114, DOI: 10.1039/D3TA04160C.

12 Z. Chu and S. Seeger, Superamphiphobic surfaces, *Chem. Soc. Rev.*, 2014, **43**, 2784–2798, DOI: 10.1039/C3CS60415B.

13 K. Seo, M. Kim and D. H. Kim, Candle-based process for creating a stable superhydrophobic surface, *Carbon*, 2014, **68**, 583–596, DOI: 10.1016/j.carbon.2013.11.038.

14 N. Y. Abu-Thabit, O. J. Uwaezuoke and M. H. Abu Elella, Superhydrophobic nanohybrid sponges for separation of oil/water mixtures, *Chemosphere*, 2022, **294**, 133644, DOI: 10.1016/j.chemosphere.2022.133644.

15 X. Zhou, Z. Zhang, X. Xu, F. Guo, X. Zhu, X. Men and B. Ge, Robust and Durable Superhydrophobic Cotton Fabrics for Oil/Water Separation, *ACS Appl. Mater. Interfaces*, 2013, **5**, 7208–7214, DOI: 10.1021/am4015346.

16 G. Ren, Y. Song, X. Li, Y. Zhou, Z. Zhang and X. Zhu, A superhydrophobic copper mesh as an advanced platform for oil-water separation, *Appl. Surf. Sci.*, 2018, **428**, 520–525, DOI: 10.1016/j.apsusc.2017.09.140.

17 M. Khosravi, S. Azizian and R. Boukherroub, Efficient oil/water separation by superhydrophobic Cu_xS coated on copper mesh, *Sep. Purif. Technol.*, 2019, **215**, 573–581, DOI: 10.1016/j.seppur.2019.01.039.

18 G. Ren, Y. Song, X. Li, Y. Zhou, Z. Zhang and X. Zhu, A superhydrophobic copper mesh as an advanced platform for oil-water separation, *Appl. Surf. Sci.*, 2018, **428**, 520–525, DOI: 10.1016/j.apsusc.2017.09.140.

19 J. Li, L. Yan, H. Li, J. Li, F. Zha and Z. Lei, A facile one-step spray-coating process for the fabrication of a superhydrophobic attapulgite coated mesh for use in oil/water separation, *RSC Adv.*, 2015, **5**, 53802–53808, DOI: 10.1039/C5RA08478D.

20 C. R. Crick, J. A. Gibbins and I. P. Parkin, Superhydrophobic polymer-coated copper-mesh; membranes for highly

efficient oil–water separation, *J. Mater. Chem. A*, 2013, **1**, 5943–5948, DOI: **10.1039/C3TA10636E**.

21 S. Wang, Y. Song and L. Jiang, Microscale and nanoscale hierarchical structured mesh films with superhydrophobic and superoleophilic properties induced by long-chain fatty acids, *Nanotechnology*, 2007, **18**, 015103, DOI: **10.1088/0957-4484/18/1/015103**.

22 R. S. Sutar, N. P. Kulkarni, S. Nagappan, A. R. Jundle, P. G. Pawar, N. N. Pargaonkar, N. B. Gharge, P. S. Yadav, S. S. Kshirsagar, S. S. Kanchankoti, A. S. Sawant, S. G. Kodag, S. S. Mahajan, V. S. Shinde, K. H. Park, K. K. Sadasivuni, A. K. Bhosale and S. S. Latthe, Octadecyltrichlorosilane-Modified Superhydrophobic-Superoleophilic Stainless Steel Mesh for Oil-Water Separation, *Macromol. Symp.*, 2021, **400**, 2100096, DOI: **10.1002/masy.202100096**.

23 D. Guo, J. Chen, K. Hou, S. Xu, J. Cheng, X. Wen, S. Wang, C. Huang and P. Pi, A facile preparation of superhydrophobic halloysite-based meshes for efficient oil–water separation, *Appl. Clay Sci.*, 2018, **156**, 195–201, DOI: **10.1016/j.clay.2018.01.034**.

24 B. K. Tudu and A. Kumar, Robust and durable superhydrophobic steel and copper meshes for separation of oil-water emulsions, *Prog. Org. Coat.*, 2019, **133**, 316–324, DOI: **10.1016/j.porgcoat.2019.04.069**.

25 J. Saengkaew, D. Le, C. Samart, H. Sawada, M. Nishida, N. Chanlek, S. Kongparakul and S. Kiatkamjornwong, Superhydrophobic coating from fluoroalkylsilane modified natural rubber encapsulated SiO_2 composites for self-driven oil/water separation, *Appl. Surf. Sci.*, 2018, **462**, 164–174, DOI: **10.1016/j.apsusc.2018.08.059**.

26 M. Zahid, G. Mazzon, A. Athanassiou and I. S. Bayer, Environmentally benign non-wettable textile treatments: A review of recent state-of-the-art, *Adv. Colloid Interface Sci.*, 2019, **270**, 216–250, DOI: **10.1016/j.cis.2019.06.001**.

27 Z. Feng, F. Wang, T. Xie, J. Ou, M. Xue and W. Li, Integral hydrophobic concrete without using silane, *Constr. Build. Mater.*, 2019, **227**, 116678, DOI: **10.1016/j.conbuildmat.2019.116678**.

28 S. Singh, D. Singh, S. P. Singh and A. K. Pandey, Candle soot derived carbon nanoparticles: Assessment of physico-chemical properties, cytotoxicity and genotoxicity, *Chemosphere*, 2019, **214**, 130–135, DOI: **10.1016/j.chemosphere.2018.09.112**.

29 L. Xiao, W. Zeng, G. Liao, C. Yi and Z. Xu, Thermally and Chemically Stable Candle Soot Superhydrophobic Surface with Excellent Self-Cleaning Properties in Air and Oil, *ACS Appl. Nano Mater.*, 2018, **1**, 1204–1211, DOI: **10.1021/acsanm.7b00363**.

30 C.-J. Liang, J.-D. Liao, A.-J. Li, C. Chen, H.-Y. Lin, X.-J. Wang and Y.-H. Xu, Relationship between wettabilities and chemical compositions of candle soots, *Fuel*, 2014, **128**, 422–427, DOI: **10.1016/j.fuel.2014.03.039**.

31 B. N. Sahoo and B. Kandasubramanian, An experimental design for the investigation of water repellent property of candle soot particles, *Mater. Chem. Phys.*, 2014, **148**, 134–142, DOI: **10.1016/j.matchemphys.2014.07.022**.

32 X. Zhang, Y. Pan, Q. Gao, J. Zhao, Y. Wang, C. Liu, C. Shen and X. Liu, Facile fabrication of durable superhydrophobic mesh *via* candle soot for oil-water separation, *Prog. Org. Coat.*, 2019, **136**, 105253, DOI: **10.1016/j.porgcoat.2019.105253**.

33 N. Celik, N. B. Kiremitler, M. Ruzi and M. S. Onses, Waxing the soot: Practical fabrication of all-organic superhydrophobic coatings from candle soot and carnauba wax, *Prog. Org. Coat.*, 2021, **153**, 106169, DOI: **10.1016/j.porgcoat.2021.106169**.

34 M. R. Mulay, A. Chauhan, S. Patel, V. Balakrishnan, A. Halder and R. Vaish, Candle soot: Journey from a pollutant to a functional material, *Carbon*, 2019, **144**, 684–712, DOI: **10.1016/j.carbon.2018.12.083**.

35 J. Song, N. Liu, J. Li, Y. Cao and H. Cao, Facile Fabrication of Highly Hydrophobic Onion-like Candle Soot-Coated Mesh for Durable Oil/Water Separation, *Nanomaterials*, 2022, **12**(5), 761, DOI: **10.3390/nano12050761**.

36 J. Yong, Y. Fang, F. Chen, J. Huo, Q. Yang, H. Bian, G. Du and X. Hou, Femtosecond laser ablated durable superhydrophobic PTFE films with micro-through-holes for oil/water separation: Separating oil from water and corrosive solutions, *Appl. Surf. Sci.*, 2016, **389**, 1148–1155, DOI: **10.1016/j.apsusc.2016.07.075**.

37 M. Martínez-Calderon, A. Rodríguez, A. Dias-Ponte, M. C. Morant-Miñana, M. Gómez-Aranzadi and S. M. Olaizola, Femtosecond laser fabrication of highly hydrophobic stainless steel surface with hierarchical structures fabricated by combining ordered microstructures and LIPSS, *Appl. Surf. Sci.*, 2016, **374**, 81–89, DOI: **10.1016/j.apsusc.2015.09.261**.

38 M. V. Rukosuyev, J. Lee, S. J. Cho, G. Lim and M. B. G. Jun, One-step fabrication of superhydrophobic hierarchical structures by femtosecond laser ablation, *Appl. Surf. Sci.*, 2014, **313**, 411–417, DOI: **10.1016/j.apsusc.2014.05.224**.

39 C. De Marco, S. M. Eaton, R. Suriano, S. Turri, M. Levi, R. Ramponi, G. Cerullo and R. Osellame, Surface Properties of Femtosecond Laser Ablated PMMA, *ACS Appl. Mater. Interfaces*, 2010, **2**, 2377–2384, DOI: **10.1021/am100393e**.

40 S. Xu, H. Dou, K. Sun, Y. Ye, Z. Li, H. Wang, W. Liao, H. Liu, X. Miao, X. Yuan, X. Jiang and X. Zu, Scan speed and fluence effects in femtosecond laser induced micro/nano-structures on the surface of fused silica, *J. Non-Cryst. Solids*, 2018, **492**, 56–62, DOI: **10.1016/j.jnoncrysol.2018.04.018**.

41 C. Fu, L. Gu, Z. Zeng and Q. Xue, One-Step Transformation of Metal Meshes to Robust Superhydrophobic and Superoleophilic Meshes for Highly Efficient Oil Spill Cleanup and Oil/Water Separation, *ACS Appl. Mater. Interfaces*, 2020, **12**, 1850–1857, DOI: **10.1021/acsami.9b17052**.

42 Wacker, *Room Temperature Vulcanizing (RTV) Silicones: Material and Processing Guidelines*, **https://www.wacker.com/h/en-us/medias/7461-EN.pdf**, accessed March 9, 2024.

43 L. Liu, H. Wang, J. Huang, M. He, S. Li, Y. Liu, F. Li and H. You, One-step fabrication of robust liquid-repellent

mesh induced by femtosecond laser, *Chem. Eng. J.*, 2023, **469**, 143853, DOI: 10.1016/j.cej.2023.143853.

44 Z. Yuan, J. Huang, C. Peng, M. Wang, X. Wang, J. Bin, S. Xing, J. Xiao, J. Zeng, X. Xiao, X. Fu, H. Gong, D. Zhao and H. Chen, Facile preparation of superhydrophobic candle soot coating and its wettability under condensation, *Appl. Phys. A: Mater. Sci. Process.*, 2016, **122**, 125, DOI: 10.1007/s00339-016-9664-z.

45 X. Wen, X. Yuan, L. Lan, L. Hao, Y. Wang, S. Li, H. Lu and Z. Bao, RTV Silicone Rubber Degradation Induced by Temperature Cycling, *Energies*, 2017, **10**(7), 1054, DOI: 10.3390/en10071054.

46 D. Cai, A. Neyer, R. Kuckuk and H. M. Heise, Raman, mid-infrared, near-infrared and ultraviolet-visible spectroscopy of PDMS silicone rubber for characterization of polymer optical waveguide materials, *J. Mol. Struct.*, 2010, **976**, 274–281, DOI: 10.1016/j.molstruc.2010.03.054.

47 T. F. Qahtan, M. A. Gondal, I. O. Alade and M. A. Dastageer, Fabrication of Water Jet Resistant and Thermally Stable Superhydrophobic Surfaces by Spray Coating of Candle Soot Dispersion, *Sci. Rep.*, 2017, **7**, 7531, DOI: 10.1038/s41598-017-06753-4.

48 G. E. Olifant, K. Kondiah and M. A. Mamo, Application of candle soot CNPs-TiO_2-PVP composite in the detection of volatile organic compounds with aldehyde, amine and ketone functional groups by resistance and impedance responses, *Nano Express*, 2021, **2**, 20010, DOI: 10.1088/2632-959X/abf60a.

49 A. J. R. Bauer, *RTV Analysis with Raman Spectroscopy*, 2018, https://tsi.com/getmedia/41f05d1f-3cca-4953-96b4-329f7d5e3970/Raman_Spectroscopic_Analysis_of_Gasket_Compounds_App_Note_RAMAN-017_US?ext=.pdf, accessed March 10, 2024.

50 G. Momen, M. Farzaneh and R. Jafari, Wettability behaviour of RTV silicone rubber coated on nanostructured aluminium surface, *Appl. Surf. Sci.*, 2011, **257**, 6489–6493, DOI: 10.1016/j.apsusc.2011.02.049.

51 H. Cao, J. Fu, Y. Liu and S. Chen, Facile design of superhydrophobic and superoleophilic copper mesh assisted by candle soot for oil water separation, *Colloids Surf., A*, 2018, **537**, 294–302, DOI: 10.1016/j.colsurfa.2017.09.055.

52 R. S. Sutar, S. S. Latthe, X. Wu, B. Shi, N. N. Pargaonkar, S. S. Ingole, A. N. Biradar, S. Nagappan, Y. H. Kim, A. K. Bhosale, V. S. Saji and S. Liu, One-step candle soot-PDMS dip-coated superhydrophobic stainless steel mesh for oil-water separation, *Mater. Lett.*, 2024, **357**, 135791, DOI: 10.1016/j.matlet.2023.135791.

53 J. Li, R. Kang, X. Tang, H. She, Y. Yang and F. Zha, Superhydrophobic meshes that can repel hot water and strong corrosive liquids used for efficient gravity-driven oil/water separation, *Nanoscale*, 2016, **8**, 7638–7645, DOI: 10.1039/C6NR01298A.

54 J. Li, Z. Zhao, R. Kang, Y. Zhang, W. Lv, M. Li, R. Jia and L. Luo, Robust superhydrophobic candle soot and silica composite sponges for efficient oil/water separation in corrosive and hot water, *J. Sol-Gel Sci. Technol.*, 2017, **82**, 817–826, DOI: 10.1007/s10971-017-4350-y.

55 R. S. Sutar, S. S. Latthe, N. B. Gharge, P. P. Gaikwad, A. R. Jundle, S. S. Ingole, R. A. Ekunde, S. Nagappan, K. H. Park, A. K. Bhosale and S. Liu, Facile approach to fabricate a high-performance superhydrophobic PS/OTS modified SS mesh for oil-water separation, *Colloids Surf., A*, 2023, **657**, 130561, DOI: 10.1016/j.colsurfa.2022.130561.

56 R. S. Sutar, S. S. Latthe, A. R. Jundle, P. P. Gaikwad, S. S. Ingole, S. Nagappan, Y. H. Kim, A. K. Bhosale, V. S. Saji and S. Liu, A facile approach for oil-water separation using superhydrophobic polystyrene-silica coated stainless steel mesh bucket, *Mar. Pollut. Bull.*, 2024, **198**, 115790, DOI: 10.1016/j.marpolbul.2023.115790.

57 A. Melnik, A. Bogoslovtseva, A. Petrova, A. Safonov and C. N. Markides, Oil–Water Separation on Hydrophobic and Superhydrophobic Membranes Made of Stainless Steel Meshes with Fluoropolymer Coatings, *Water*, 2023, **15**(7), 1346, DOI: 10.3390/w15071346.

58 O. Rius-Ayra and N. LLorca-Isern, Growth of a superhydrophobic coating on an aluminium substrate with strong adhesive properties and showing efficient oil/water separation, *Thin Solid Films*, 2020, **710**, 138259, DOI: 10.1016/j.tsf.2020.138259.